Robotica (2017) volume 35, pp. 521–536. © Cambridge University Press 2015
doi:10.1017/S0263574715000697

Design, analysis, and testing of a motor-driven capsule robot based on a sliding clamper

Jinyang Gao*, Guozheng Yan, Su He, Fei Xu and Zhiwu Wang

Department of Instrument Science and Engineering, Shanghai Jiaotong University, No. 800 Dongchuan Road, Shanghai, P. R. China

(Accepted July 22, 2015. First published online: August 17, 2015)

SUMMARY

We propose a motor-driven capsule robot based on a sliding clamper (MCRSC), a device to explore the partially collapsed and winding intestinal tract. The MCRSC is powered by wireless power transmission based on near-field inductive coupling. It comprises a novel locomotion unit, a camera, and a three-dimensional receiving coil, all installed at both ends of the locomotion unit. The novel locomotion unit comprises a linear motion mechanism and a sliding clamper. The former adopts a pair of lead-screw and nut to obtain linear motion, whereas the latter anchors the MCRSC to a specific point of the intestinal tract by expanding its arc-shaped legs. The MCRSC is capable of two-way locomotion, which is activated by alternately executing linear motion and anchoring action. *Ex vivo* experiments have shown that the MCRSC is able to inspect the colon within a time frame of standard colonoscopy.

KEYWORDS: Intestinal tract; Capsule robot; Linear motion mechanism; Sliding clamper; Micro robotics.

1. Introduction

Introduction of wireless capsule endoscopy (WCE), developed by Given Imaging Ltd.[1] (Yoqneam, Israel), represents a milestone in the evolution of endoscopy. Compared with conventional endoscopy, WCE enables a safer and more comfortable diagnosis, avoids complications and hazards such as perforation,[2]and can inspect the formerly unreachable jejunum and ileum. Importantly, WCEs are propelled by natural intestinal peristalsis, which leads to a low diagnostic yield for some important intestinal tract regions.[3]Capsule robot (CR) has been developed as an enhanced substitute for WCEs.[4–23] Capsule robot integrates an active locomotion unit, by which advanced diagnostic or therapeutic functions, such as drug delivery[6] and tissue sampling[7], can be realized.

Current capsule robots employ one of the two types of actuation, depending on their target organs. Magnetically driven capsule robots,[5–10] which are actuated by magnetic interaction between on-board permanent magnets and external steerable magnetic field, are designed for gastric endoscopy because three-dimensional (3D) motion is required, and there is no significant friction between the moving capsule robots and the stomach wall. On the other hand, capsule robots having on-board actuators[12–23] are designed for intestinal endoscopy because a strong propulsive force is needed to overcome friction in collapsed regions.

A lot of on-board actuator-based capsule robots have emerged in the past few years. Legged capsule robots[12,13] feature a swallowable size, and normally adopt two brushless motors to actuate two sets of superelastic legs, which have the double function of enabling locomotion and distending the collapsed intestinal tissue for better inspection. However, the two motors need to be powered simultaneously for a fixed period in a full gait cycle. Thus, the power source must be able to output a peak power of at least 400 mW. Currently, the most promising power source that can power the capsule robot system for a

* Corresponding author. E-mail: gjy.1001@163.com

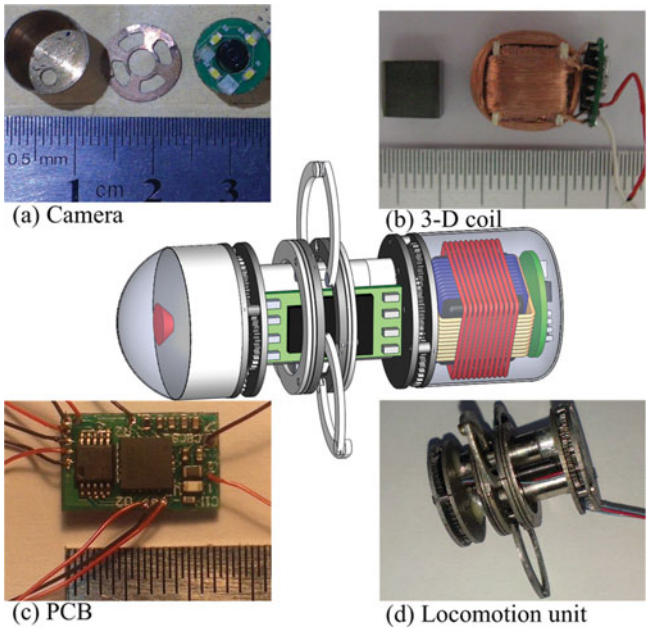

Fig. 1. Design overview of wireless powered MCRSC: (a) front-facing camera, (b) 3D receiving coil to power MCRSC, (c) PCB for communication and control, and (d) assembled prototype of locomotion unit.

long duration is based on wireless power transmission (WPT),[24] but the high peak power required to power legged capsule robots significantly increases the difficulty in the design and implementation of the WPT system and hinders integrating other power-consuming functionalities. The paddling-type capsule robot,[14] although has a high speed of 17 cm/min in the colon, can only navigate in one direction, and is unable to hold itself at suspicious lesions, so it is suitable to be served only as an inspecting device for the colon. Inchworm-like capsule robots have been developed for decades from the initial tether devices[15–17] to the recent tether-less devices.[18–20] The tether devices have a limitation of a short travel distance in the intestinal tract, while the tether-less devices normally have retracted lengths of over 50-mm threshold, which other types of capsule robots do not exceed[5–14,21–23] and results in poor performance when passing through the tight bends of the intestinal tract. The tank-like capsule robot[21] adopts four pairs of micro-patterned treads to enable locomotion on a planar tissue surface or in the collapsed cecum lumen, and based on a thorough analysis of adhesivity between the intestinal mucosa and employed materials,[25,26] a method for optimizing the design of the threads has been proposed. However, the tank-like capsule robot is also a tether device, but being limited by current engineering technology, reducing its size to a swallowable level is very difficult.

To address the aforementioned limitations of the currently existing capsule robots with on-board actuators, we propose a motor-driven capsule robot based on a sliding clamper (MCRSC). The MCRSC is powered by WPT based on a near-field inductive coupling. It comprises a novel locomotion unit, a camera, and a 3D receiving coil, all installed at both ends of the locomotion unit. This paper presents the design and analysis of the proposed MCRSC and the focus is on the novel locomotion unit. *Ex vivo* experiments have shown that the proposed MCRSC is able to inspect the colon within the time frame of a standard colonoscopy.

This paper is organized as follows: Section 2 provides details about the design and fabrication of MCRSC; Section 3 focuses on kinetic analysis; Section 4 tests the performance of the proposed MCRSC; and Section 5 concludes.

2. Design and Fabrication

2.1. Design overview

Figure 1 shows the design overview of the wireless powered MCRSC, which has a diameter of 14-mm and a length of 40 mm.

https://doi.org/10.1017/S0263574715000697 Published online by Cambridge University Press

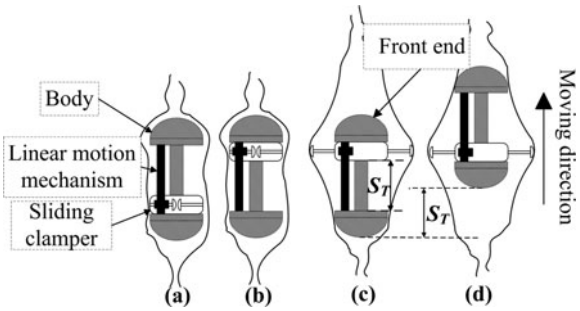

Fig. 2. Locomotion principle of MCRSC.

Figure 1(a) shows the front-facing camera, which could capture images of the intestinal tract with a resolution of 320 × 240, transform the images into National Television System Committee (NTSC) video sequences with a frame rate of 30 frames per second, and transmit video sequences to an external video display device in a wireless mode for diagnosis. This camera has a power consumption of 69 mW and is housed in a copper shell, measuring 10 mm in diameter and 6 mm in length, to achieve magnetic shield.

Figure 1(b) shows the 3D receiving coil, which is constructed by winding Litz wire on a high permeability MnZn ferrite core with a size of 7 × 7 × 7 mm, and the number of turns of each dimension is 80. To avoid thermal burn of the intestinal tissue caused by rise in temperature of 3D receiving coil, Litz wire twined with 12 strands of AWG 44-enameled copper wire is adopted to reduce power dissipation on 3D receiving coil.[24] This 3D receiving coil, together with a full-bridge rectifier that is fixed on its one side, occupies a space of Φ12 × 13 mm. When the transmitting coil is a double-layer solenoid pair (400 mm in diameter) and the transmission frequency is 218 KHz,[24] the output power of this 3D receiving coil could achieve 536 mW under the worst conditions, which basically meets the power requirement of MCRSC.

Figure 1(c) shows the printed circuit board (PCB) for communication and control, and measures 12 × 8 × 3.2 mm.

Figure 1(d) shows the assembled prototype of the novel locomotion unit, which measures 14 mm in diameter and 20.4 mm in length. The locomotion unit comprises a linear motion mechanism that enables linear motion, and a sliding clamper that could anchor MCRSC to a specific point of the intestinal tract. Two brush-DC motors (QX4A1-080071 and QX4A3-065131),[27] both measuring Φ4 × 12 mm, are powered in turn to activate linear motion and anchoring action alternately, by which two-way locomotion is obtained. In addition, the sliding clamper, which has a fully leg-expanding diameter of 32.6 mm, could distend the collapsed tissue to enhance visualization or hold MCRSC at suspicious lesions for a detailed inspection. In addition to the front-facing camera, the locomotion unit could also carry a tissue sampling mechanism,[28] or a chamber that stores medicament,[6,29] or an optical biopsy device, to fulfill specific diagnostic or therapeutic application.

Figure 2 shows the locomotion principle of MCRSC: Step (a) shows the initial state of MCRSC; in step (b), the sliding clamper slides forward under the actuation of linear motion mechanism; in step (c), the sliding clamper expands its legs and anchors to a specific point; in step (d), the linear motion mechanism propels the body (i.e., gear reducers at both ends and two on-board DC motors) to stroke S_T. A repetitive sequence of these steps advances the MCRSC, and a repetitive inverted sequence makes it retreat. This locomotion principle inspires several design rules, which are as follows:

(1) As shown in steps (a) and (b), tissue might be deformed and folded into the MCRSC because of the friction between the sliding clamper and the intestinal wall; thus, the diameter of the sliding clamper should be smaller than that of the body to diminish this friction.

https://doi.org/10.1017/S0263574715000697 Published online by Cambridge University Press

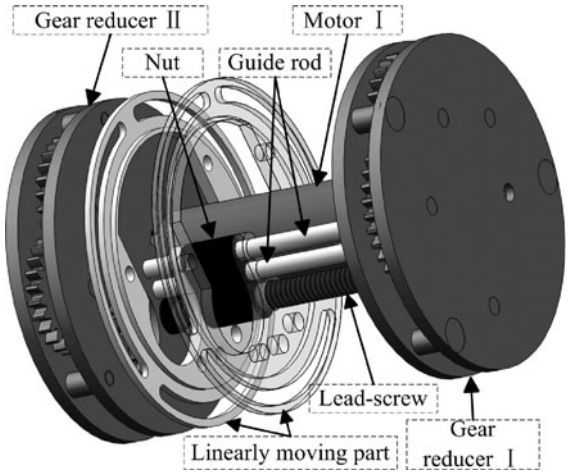

Fig. 3. Design showing the linear motion mechanism.

(2) As shown in step (c), to ensure passing and anchoring in different regions of the intestinal tract, the sliding clamper should have a large expanding ratio (i.e., the ratio between its fully leg-expanding and leg-retracting diameters).
(3) As shown in steps (c) and (d), a large-enough expanding diameter may help avoid stroke loss by reducing environmental resistance[22] exerted on the front end.
(4) To obtain a higher stroke ratio (i.e., ratio between the lengths of the periodic stroke and the MCRSC), gear reducers and sliding clamper should be as compact as possible in a longitudinal direction.

2.2. Linear motion mechanism design

A detailed design of the linear motion mechanism is shown in Fig. 3, and the design parameters of lead-screw and nut are presented in Table I. The output torque of motor I is amplified by gear reducer I, and then rotates the lead-screw. The linearly moving parts are the components of the sliding clamper, and their functions are illustrated in the next section. When the sliding clamper retracts its legs, it will be translated by the nut; when the sliding clamper expands its legs and anchors to a specific point, the body will be translated by the lead-screw. Two guide rods are employed to smooth the linear motion.

2.3. Sliding clamper design

To obtain a large expanding ratio, we propose an arc-shaped leg design, which enables an expanding ratio by over 230%. Another key design feature of the sliding clamper is annular gear transmission, which is compact in longitudinal direction and offers a high transmission ratio.

A detailed design showing the sliding clamper is given in Fig. 4, and its design parameters are given in Table I. As in Fig. 4(a), the output torque of motor II is first amplified by gear reducer II, and then rotates a D-shaft. When the D-shaft has been rotated as indicated by the curved arrow labeled on it, the sliding clamper expands arc-shaped legs. Figure 4(b) is the cutaway view of the sliding clamper. A spur pinion I with a D-shaped hole is connected to the D-shaft, and meshes simultaneously with a spur pinion II and an annular gear I; then the spur pinion II meshes with an annular gear II. Figure 4(c) shows the top view of the leg-expanding process for a pair of legs: leg I is hinged to the annular gears I, and leg II is hinged to the annular gears II (not shown). When the spur pinion I is actuated to rotate in counterclockwise direction, the annular gear I also rotates counterclockwise but the annular gear II rotates clockwise, enabling the sliding clamper to expand its legs; conversely, the sliding clamper retracts its legs when the spur pinion I rotates clockwise. Since the parameters of the spur pinion I and the annular gear I are identical respectively to those of the spur pinion II and the annular gear II, these two annular gears rotate equally in magnitude and oppositely in direction, which makes the hinge point of legs I and II expand along a radial locus. The radial leg-expanding function avoids scratching tissue and enables a safe tissue–leg interaction. In addition, each pair of legs forms

https://doi.org/10.1017/S0263574715000697 Published online by Cambridge University Press

Table I. Design parameters of MCRSC.

Motor I(II)	Length	12 mm	
	Diameter	4 mm	
	Speed	$r_{MI(II)} = 26{,}200$ (23,400) rpm	
	Rated-voltage	3 V	
	Stall torque	$T_{MI(II)} = 1.39$ (0.83) gf· cm	
Linear motion mechanism	Lead-screw	Nominal diameter	$d = 1.2$ mm
		Thread angel	$\alpha = 60^{\circ}$
		Pitch	$p = 0.25$ mm
		Thread length	$L_{\text{thread}} = 13$ mm
	Nut	Length	$L_{\text{nut}} = 2.6$ mm
Sliding clamper	Spur pinion I(II)	Modulus	0.2
		Teeth number	$z_s = 9$
	Annular gear I(II)	Modulus	0.2
		Teeth number	$z_A = 54$
Gear reducer I	Modulus	0.2	
	Total stages	$s_{\text{I}} = 4$	
	Reduction ratio	$n_{\text{I}} = 40.31{:}1$	
Gear Reducer II	Modulus	0.2	
	Total stages	$s_{\text{II}} = 6$	
	Reduction ratio	$n_{\text{II}} = 296.4{:}1$	

a closed hinge separately, and the potential risk of tissue entrapment in the device's mechanism is minimized accordingly.

When the sliding clamper expands or retracts its legs, the two annular gears should only reserve rotational degree of freedom (DOF) about longitudinal axis to ensure a stable leg-expanding or leg-retracting process. To achieve this, two extra parts, a linearly moving part and an abdeckring, are designed, as shown in Fig. 4(d). We assembled screw I through the countersink of annular gear I, the arc-shaped groove of the linearly moving part, and the screw hole of abdeckring in sequence. Thus, when the position of the linearly moving part is fixed by the linear motion mechanism, each of the annular gears only has a rotational DOF about the longitudinal axis. In addition, the radian of the arc-shaped groove machined in the linearly moving part sets the rotating angle range. Hundreds of 0.35-mm diameter balls are employed between two parts of each annular gear, linearly moving part, and abdeckring to implement rolling friction. To supply more space for system integration, we only reserve a quarter of teeth for two annular gears, as shown in Fig. 4(c). Finally, the two linearly moving parts are fixed together with a union nut, as shown in Fig. 4(b).

The assembled sliding clamper is shown in Fig. 4(e), with a longitudinal thickness of 4.96 mm, fully leg-expanding and leg-retracting diameters of 32.6 mm and 13.62 mm, respectively; when fully expanded, it looks somewhat like a clover.

2.4. Fabrication

All mechanical parts of MCRSC were fabricated in-house using a slow-feeding electrical discharge machine, a turning-lathe, and a hardening furnace with type-304 stainless steel or aluminum alloy, both of which are biocompatible with the human intestinal tract environment. Mechanical parts that required structural stiffness (e.g., legs, gears, and baffles) were produced from type-304 stainless steel; other mechanical parts were constructed with aluminum alloy to minimize the total weight of MCRSC. To increase the surface hardness and wearability of gears, they still needed to undergo an extra hardening operation.

For a long-term stable operation of MCRSC, several design details shown in Fig. 5 are also notable. As in Fig. 5(a), the micro-spring (with both wire diameter and pitch of 0.2 mm, outer diameter of 1.8 mm, spring constant of 3 N/mm, and having 4 turns) was fitted around the guide rod, which increases longitudinal load when the sliding clamper slides to both ends of MCRSC; then the increased current of the DC motor that is detected by a current-sense chip (MAX 4173) could provide a position reference for linear motion. Another function of the micro-spring is to provide a minimum clearance

https://doi.org/10.1017/S0263574715000697 Published online by Cambridge University Press

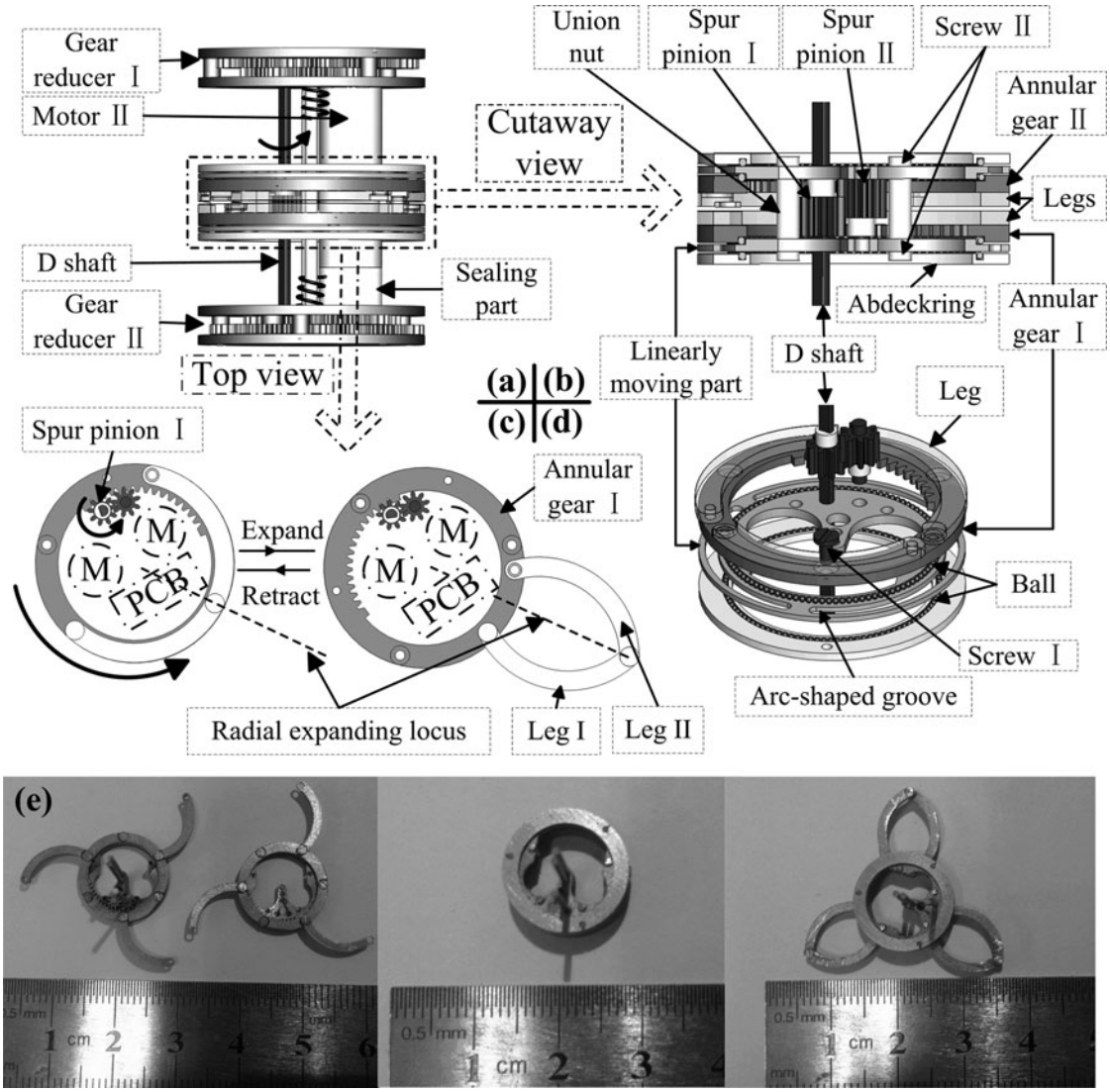

Fig. 4. Design details showing of the sliding clamper: (a) design overview of the sliding clamper, (b) cut away view of the sliding clamper, (c) top view of the leg-expanding process for a pair of legs, (d) fixation of annular gears for a stable leg-expanding process, and (e) assemble prototype of the sliding clamper.

of 0.3 mm (i.e., when the micro-spring is completely compressed by the baffle and the linearly moving part) between the abdeckring and the baffle of the gear reducer, thereby avoiding sliding friction when the sliding clamper expands or retracts its legs. As in Fig. 5(b), two wear-resistant parts were specially designed to handle the abrasion of lead-screw with a thread height of only 0.162 mm. Wear-resistant part I and part II were installed at the baffle and the lead-screw, respectively, with interference fit; these were fabricated with type-304 stainless steel, and were subjected to a hardening operation. To reduce frictional coefficient, we machined a groove to store lubricant on wear-resistant part II. As in Fig. 5(c), motor was sealed with a sealing part and a die-sinking fluorine rubber gasket with a thickness of 0.1 mm; the inner diameter of the gasket (0.68 mm) is smaller than that of the motor shaft (0.7 mm). We first glued the gasket to the ring groove of the sealing part, and then glued the sealing part and motor with epoxy adhesive. Output torque loss induced by friction between the gasket and the motor shaft was measurably negligible. We immersed several sealed motors in water, and controlled them to rotate clockwise for 1 h and counterclockwise for an additional hour. The devices have no short-circuit faults during this testing, demonstrating the feasibility of this sealing method.

https://doi.org/10.1017/S0263574715000697 Published online by Cambridge University Press

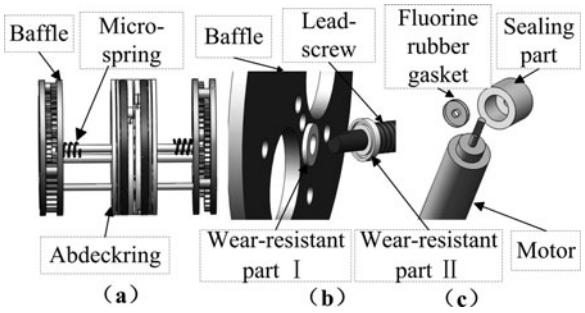

Fig. 5. Other notable design details: (a) micro-spring, (b) wear-resistant design of lead-screw, and (c) sealing method for motors.

3. Kinetic Analysis

We present a detailed kinetic analysis for MCRSC in this section. To explore the intestinal tract effectively, capsule robots must meet several kinetic requirements, e.g., the leg-expanding force of the sliding clamper must be large enough to expand the surrounding intestinal tissue, and the longitudinal thrust generated by the linear motion mechanism must be sufficient for counteracting friction in the collapsed intestines.

Normally, a total leg-expanding force of 3 N and a longitudinal thrust of 6 N are sufficient for capsule robots that explore the colon.[12,23] The leg-expanding time should be the best compromise between the safety of tissue–leg interaction and the locomotion efficiency. In other words, if the legs expand too quickly, the intestinal stimulation may cause discomfort to the patient; if the legs expand too slowly, the velocity of MCRSC would be decreased. Referring to a 1.8-s leg-expanding time selected by Woods and Constandinou,[29] we set it between 1 and 2 s. To fulfill the above requirements, gear reducers I and II need to be carefully designed. Satisfactory design parameters are given in Table I.

The intestinal tract is not completely horizontal when the patient lies down. The natural state of the intestinal tract, which connects to the abdominal wall through the mesentery, is freely suspended,[30] so some slopes form unavoidably. In addition, the sliding clamper is in fully leg-retracting state in steps (a) and (b), and gravity may glide it in this stage. For these reasons, we introduce a dedicated analysis to assess the climbing performance of MCRSC.

The symbols used in the analysis below are identical to those shown in Table I.

3.1. Linear motion mechanism analysis

The translational speed of the sliding clamper or the body is computed as

$$v_L = r_{MI} p / n_{\mathrm{I}}. \tag{1}$$

However, a higher v_L would bring about a higher frictional resistance,[31] so we set $v_L \leq 5$ mm/s here.

The longitudinal thrust f_L could be calculated from torque balance analysis:

$$T_{\mathrm{lead-screw}} = T_{\mathrm{fri}}, \tag{2a}$$

where $T_{\mathrm{lead-screw}}$ is the driving torque of lead-screw, which is the output torque of motor I amplified by gear reducer I; and T_{fri} is the friction torque of lead-screw when a longitudinal resistance is exerted on the nut. $T_{\mathrm{lead-screw}}$ and T_{fri} could be computed with the below expressions, respectively[32]:

$$T_{\mathrm{lead-screw}} = T_{MI} n_{\mathrm{I}} \eta_{\mathrm{I}}^{s_{\mathrm{I}}}, \tag{2b}$$

$$T_{\mathrm{fri}} = f_{\mathrm{Lris}} \frac{d}{2} \left[\tan(\psi + \rho_v) + \frac{\mu \pi a}{L_{\mathrm{nut}} \sin(\alpha/2)} \right], \tag{2c}$$

https://doi.org/10.1017/S0263574715000697 Published online by Cambridge University Press

Table II. Design of the gear reducer I.

Design objective	max v_L, min s_{I}			
Design constraint	$v_L \leq 5$ mm/s, $f_L \geq 6$ N			
Design parameters				
No. of stages	1	2	3	4
No. of teeth on driver	9	9	9	9
No. of teeth on follower	19	24	29	20
Total layers	2			

where $T_{M\mathrm{I}}$, n_{I}, d, L_{nut}, and α are defined in Table I, η_{I} is the transmission efficiency of each stage in gear reducer I, its value is selected as 0.92 in computing; s_{I} is the total stages of gear reducer I; f_{Lris} is the longitudinal resistance exerted on the nut; ψ is the helix angle, and is computed as $\psi = \arctan(p/\pi d)$, and p is the pitch of lead-screw; ρ_v is the equivalent friction angle, and is computed as $\rho_v = \arctan(\mu/\cos(\alpha/2))$, μ is the coefficient of sliding friction between lead-screw and nut with a value of 0.13; a is the distance between the central axis of lead-screw and that of the body with a value of 2.512 mm in this design. From Eqs. (2a), (2b), and (2c), we could obtain the longitudinal resistance f_{Lris}, which is equal to the longitudinal thrust f_L.

Table II shows the design process of gear reducer I. We chose the design objective shown in Table II because a higher v_L improves inspecting efficiency and a smaller s_{I} diminishes energy loss caused by friction between gears. Combining design constraints and Eqs. (1), (2a), (2b), and (2c), we can compute a reduction ratio range for gear reducer I. After accounting for the position of the motor shaft input and the lead-screw output, and the limitation of available space for gear reducer I, the finally design parameters of gear reducer I can be determined, which corresponds to a reduction ratio, $n_{\mathrm{I}} = 40.31 : 1$ (shown in Table I). Then the theoretical values of v_L and f_L are computed to be 2.7 mm/s and 6.6 N, respectively.

3.2. Sliding clamper analysis

The sliding clamper could be equivalent to a four-bar linkage, as shown in Figs. 6(a) and (b). Points $A(A')$, $B(B')$, and $C(C')$ are hinge joints; Leg_{AB}, Leg_{CB}, and annular gears I and II are equivalent to rigid rods 1, 3, 2, and 4, respectively. The rotating center $D(E)$ is the geometric center of the annular gear I(II), and the revolving speed $\omega_2(\omega_4)$ of rigid rod 2(4) is just that of the annular gear I(II).

We use l_{AB}, l_{DA}, l_{CB}, and l_{EC} to represent the length of rigid rods 1, 2, 3, and 4, respectively; the corresponding azimuths φ_1, φ_2, φ_3, and φ_4 are written as follows:

$$\begin{cases} \varphi_1(t) = a\cos\left(\dfrac{l_{AB}^2 + l_{AC}^2 - l_{\mathrm{CB}}^2}{2l_{AB}l_{AC}}\right) \\ \varphi_2(t) = \varphi_2(0) + \omega_2 t \\ \varphi_3(t) = \pi - \varphi_1(t) \\ \varphi_4(t) = \varphi_4(0) + \omega_4 t \\ l_{AC} = \sqrt{l_{DA}^2 + l_{EC}^2 - 2l_{DA}l_{EC}\cos[\varphi_2(t) - \varphi_4(t)]} \\ |\omega_2| = |\omega_4| = \dfrac{r_{M\mathrm{II}} z_S}{n_{\mathrm{I}} z_A} \end{cases}. \tag{3}$$

We express the position vector of hinge joint B as

$$\mathbf{r_B} = l_{DA}e^{i\varphi_2} + l_{AB}e^{i\varphi_1}. \tag{4}$$

Then the expanding speed is obtained from Eq. (4) by taking the derivative of time

$$\mathbf{v_B} = d\mathbf{r_B}/dt. \tag{5}$$

https://doi.org/10.1017/S0263574715000697 Published online by Cambridge University Press

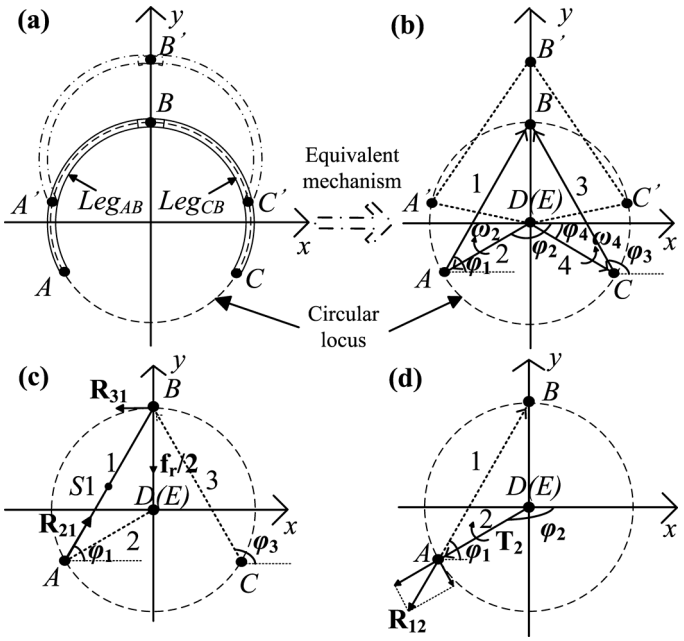

Fig. 6. Kinetic analysis of the sliding clamper: (a) leg-expanding process of a pair of legs, (b) equivalent four-bar linkage, (c) equilibrium analysis of rigid rod 1, and (d) equilibrium analysis of rigid rod 2.

The sliding clamper suffers increasing tissue resistance $\mathbf{f_r}$ in the leg-expanding process; when $\mathbf{f_r}$ is equal to the leg-expanding force $\mathbf{F_r}$ generated by the sliding clamper, the equilibrium state is achieved. The torques of rigid rods 2 and 4 are respectively denoted by $\mathbf{T_2}$ and $\mathbf{T_4}$, whose numerical values are computed with the following equation:

$$T_2 = T_4 = \frac{1}{2} T_{M\text{II}} n_{\text{II}} (\eta_{\text{II}1})^{s_{\text{II}}} \frac{z_A}{z_s} \eta_{\text{II}2}, \tag{6}$$

where $\eta_{\text{II}1}$ equaling to η_{I} is the transmission efficiency of each stage in gear reducer II, $\eta_{\text{II}2}$ is the transmission efficiency from the D-shaft to the annular gears I and II with a value of 0.79, which is computed with the measurements obtained by two torque meters (TOHNICHI-ATG09CN) placed at the input, i.e., the D-shaft, and the output, i.e., the annular gears (or the abdeckrings), respectively. Two extra auxiliary devices are necessary to make the size of D-shaft and annular gears (or abdeckrings) compatible with the anchoring range of the torque meter.

Provided that the friction in hinge joints is negligible, when force equilibrium $\sum \mathbf{F} = 0$ and moment equilibrium $\sum \mathbf{T} = 0$ are exerted on rigid rod 1 (as shown in Fig. 6(c)), we obtain

$$\begin{cases} \mathbf{R_{21}} + \mathbf{R_{31}} + \mathbf{f_r}/2 = 0 \\ \mathbf{l}_{S1A} \times \mathbf{R_{21}} + \mathbf{l}_{S1B} \times \mathbf{R_{31}} + \mathbf{l}_{S1B} \times \mathbf{f_r}/2 = 0 \end{cases}, \tag{7}$$

where $\mathbf{R_{ij}}$ is the force of rigid rod i acting on rigid rod j, $\mathbf{l}_{S1A(b)}$ is the vector from point $S1$ to point $A(B)$.

When moment equilibrium $\sum \mathbf{T} = 0$ is exerted on rigid rod 2 (as shown in Fig. 6(d)), we obtain

$$\mathbf{l}_{DA} \times \mathbf{R_{12}} + \mathbf{T_2} = 0. \tag{8}$$

Then the numerical value of the leg-expanding force $\mathbf{F_r}$ could be derived from (6), (7), and (8):

$$F_r = -f_r = \frac{2T_2}{(y_A \tan\varphi_2 + x_A)}, \tag{9}$$

where x_A and y_A are the position coordinates of hinge joint A.

https://doi.org/10.1017/S0263574715000697 Published online by Cambridge University Press

Table III. Design of the gear reducer II.

Design object			min s_{II}			
Design constraint			1 s $\leq \Phi/\omega_2 \leq$ 2 s, $F_r \geq$ 3 N			
			Design parameters			
No. of stages	1	2	3	4	5	6
No. of teeth on driver	9	9	9	9	9	9
No. of teeth on follower	15	20	25	30	35	20
Total layers			2			

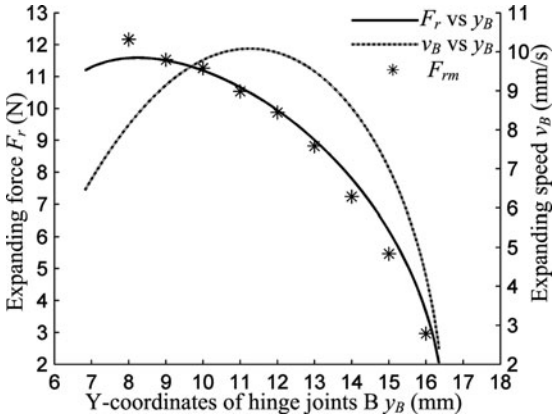

Fig. 7. Relation of expanding speed v_B and force F_r versus the position of hinge joint B y_B, andF_{rm} is the measuring value of expanding force.

Table III shows the design process of gear reducer II, which is similar to that of gear reducer I. Here we set a leg-expanding time of 1–2 s as a design constraint, and it could be expressed as Φ/ω_2, where $\Phi = 95^\circ$ is the radian of the arc-shaped groove of the linearly moving part. The design parameters of gear reducer II are shown in Table III, which correspond to a reduction ratio, $n_{II} = 296.4{:}1$ (shown in Table I) and a leg-expanding time of 1.2 s.

Now we can obtain the relation of expanding speed and expanding force versus the position of hinge joint B, as shown in Fig. 7. This curve graph could better our understanding of tissue–leg interaction process: legs and the surrounding tissues begin to interact with each other at $y_B = 10$–15 mm (the lumen diameter of the colon is typically 20–30 mm)[33]; when $y_B > 15$ mm, both expanding speed and expanding force have decreased to relative small values, which are beneficial to avoid intestinal injury caused by excessive expanding.

3.3. Climbing performance analysis

External forces acting on MCRSC in different locomotion steps are shown in Fig. 8. G is the gravity of MCRSC, and its tangential component is denoted by G_t; N is the normal force; f is the maximum static friction; f_c is the sliding friction acting on the sliding clamper in step (b) and f_b is the sliding friction acting on the body in step (d); and F_c is the anchoring force. We also denote the tangential force generated by the tangential deflections of tissue as F_t (i.e., for a deflection of D_t, the corresponding tangential force will be $F_t(D_t)$ and *vice versa*); the force–deflection relationship could refer to the hyperelastic model or the biaxial mechanical model.[34,35] In addition, the force analysis for different locomotion steps shown below is based on the contact model of tangential compliance.[36]

Equations (10) give the critical condition of slipping in different locomotion steps, and the superscripts denote the corresponding locomotion steps. Here we assume that the anchoring force is always sufficient to ensure anchoring. Climbing is considered to have failed if slipping occurs when the sliding clamper is in fully leg-retracting state, or if the effective periodic stroke $S_{net} = 0$.

$$\begin{cases} \max f^a \geq G_t = F_t(D_t^a) & \text{no slipping} \\ \max f^a < G_t & \text{slipping} \end{cases}, \tag{10a}$$

https://doi.org/10.1017/S0263574715000697 Published online by Cambridge University Press

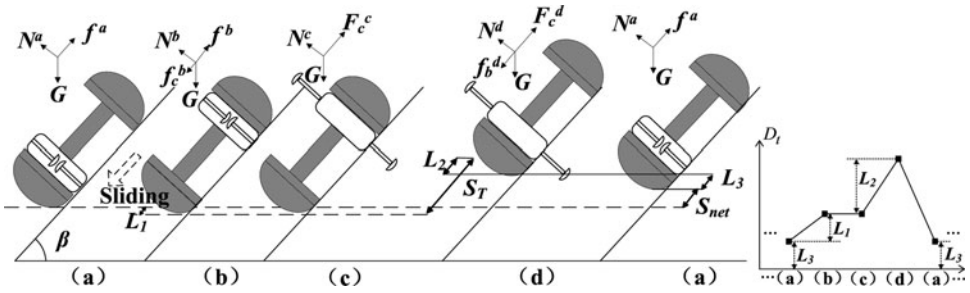

Fig. 8. External forces acting on MCRSC, and the lower right shows the changing of the tissue's tangential deflections, D_t, in different locomotion steps.

$$\begin{cases} \max f^b \geq G_t + f_c^b = F_t(D_t^b) & \text{no slipping} \\ \max f^b < G_t + f_c^b & \text{slipping} \end{cases}, \tag{10b}$$

$$\begin{cases} \max F_c^c \geq G_t = F_t(D_t^c) & \text{no slipping} \\ \max F_c^c < G_t & \text{slipping} \end{cases}, \tag{10c}$$

$$\begin{cases} \max F_c^d \geq G_t + f_b^d = F_t(D_t^d) & \text{no slipping} \\ \max F_c^d < G_t + f_b^d & \text{slipping} \end{cases}. \tag{10d}$$

According to Eqs. (10), we could easily judge that slipping is most likely to occur in step (b) because the tangential force $F_t(D_t^b)$ is larger than that in step (a), while the maximum static friction f^b is the same as that in step (a). Then the maximum angle of slope, $\max \beta_1$, for no slipping could be calculated from the expression given below:

$$f^b = G_t(\max \beta_1) + f_c^b. \tag{11}$$

Figure 8 shows that the effective periodic stroke S_{net} is related to stroke losses L_1, L_2, and L_3, which happen in steps (b), (d), and (a), respectively:

$$\begin{cases} S_{\text{net}} = S_T - L_1 - L_2 - L_3 \\ L_1 = D_t^b - D_t^a \\ L_2 = D_t^d - D_t^c \\ L_3 = D_t^a \end{cases}. \tag{12}$$

Stroke loss L_1 is negligible because f_c^b is usually very small. Stroke loss L_2 is generated by tissue stretching between the sliding clamper and the front end, and it is usually the primary loss for both climbing and horizontal cases. Several methods could rectify this loss, such as minimizing the length of both ends and optimizing the shape of the front end to decrease environmental resistance. Stroke loss L_3 is only related to G_t. We use $\max \beta_2$ to denote the maximum angle of slope for a positive net stroke. When we substitute the tangential deflections D_t solved in Eqs. (10) into Eq. (12) and set the effective stroke, $S_{\text{net}} = 0$, the equation governing $\max \beta_2$ can be obtained as follows:

$$S_{\text{net}} = S_T - F_t^{-1}[G_t(\max \beta_2) + f_c^b] - F_t^{-1}[G_t(\max \beta_2) + f_b^d] + F_t^{-1}[G_t(\max \beta_2)] = 0. \tag{13}$$

Now the maximum angle of slope for effective climbing can be expressed as:

$$\max \beta = \min[\max \beta_1, \max \beta_2]. \tag{14}$$

The climbing performance of MCRSC is considered inferior to capsule robots that continuously anchor to the intestinal wall when $\max \beta = \max \beta_1$; by contrast, it is considered comparable or even better when $\max \beta = \max \beta_2$. For example, the stroke loss induced by gravity occurs twice in a single locomotion cycle for a two-cell earthworm,[36] whereas it occurs only once for MCRSC. In

https://doi.org/10.1017/S0263574715000697 Published online by Cambridge University Press

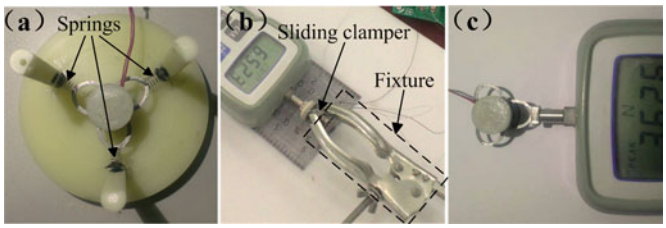

Fig. 9. Bench test: (a) measuring the fully leg-expanding and leg-retracting time, (b) measuring the longitudinal thrust, and (c) measuring the leg-expanding force.

addition, we find that max β is closely related to the weight of MCRSC from Eqs. (11) and (13); thus, minimizing the weight of MCRSC is necessary to improve its climbing performance.

The gravity G in this climbing analysis could be replaced with other external forces; thus, this analytic methodology could be applied to any case in which the MCRSC would need to withstand external resistances.

4. Experiments

4.1. Bench test

Two sets of bench tests were conducted to assess whether the action speed and mechanical features of the prototype met the design specifications.

The action speed was measured with a common stopwatch. A dedicated apparatus with three circularly equi-spaced springs was used to simulate tissue resistance during the leg-expanding process, as shown in Fig. 9(a). The springs used here were 0.2 mm in wire diameter, 4.5 mm in outer diameter, 9 mm in length, and have a spring constant of 0.18 N/mm. These were glued to three equi-spaced rods fixed in a circle of 38-mm diameter. Therefore, the legs would begin to interact with the springs at a leg-expanding diameter of 20 mm, and when the legs expanded to a maximum diameter of 32.6 mm, the springs would withstand a compression of 6.3 mm, which would translate into a 1.1-N resistance for each pair of legs. The average time for leg-expanding and leg-retracting processes was 1.13 s and 0.67 s, respectively; the average time for the one-way linear motion was 2.31 s, which corresponded to a translational speed of 3.68 mm/s. Errors between the measured values and the theoretical ones were caused by the difference between the actual revolving speed of DC motor and the revolving speed adopted in theoretical analysis. For DC motor, its revolving speed will decrease with increase in the required output torque, which increases with the encountered external resistance. In spite of obvious errors, the measured action speed still meets the design specifications defined in Tables II and III.

The mechanical features were measured with a force gauge (SHIMPO FGC-0.5B). Figure 9(b) shows the measurement of longitudinal thrust: first the sliding clamper was fixed by a fixture, and then the linear motion mechanism was activated to translate the body of MCRSC to push force gauge. Similarly, the leg-expanding force was measured by first fixing the body and then activating the sliding clamper to expand its legs against the force gauge, as shown in Fig. 9(c). The mechanical features also met the design requirements: the maximum longitudinal thrust was 6.5 N; the measurements of the leg-expanding force, F_{rm} (see Fig. 7), agreed well with the theoretical ones, and when the leg-expanding diameter was 32 mm, the measured leg-expanding force was 2.964 N, which is basically equal to the required force of 3 N.

4.2. Ex vivo experiments

The intestinal samples were excised from a pig weighing about 130 kg, which closely resembled that of human body.[37] These were stored in a refrigerated physiological saline solution to preserve biomechanical properties before testing. To maintain tissue hydration during testing, the intestinal sample was humidified with 2-mL solution every 3–5 min.

4.2.1. Measurement of anchoring force. As shown in Fig. 10(a), the anchoring force was measured with a force gauge (SHIMPO-FGC-0.5B) installed at a super linear guide. The force gauge could

https://doi.org/10.1017/S0263574715000697 Published online by Cambridge University Press

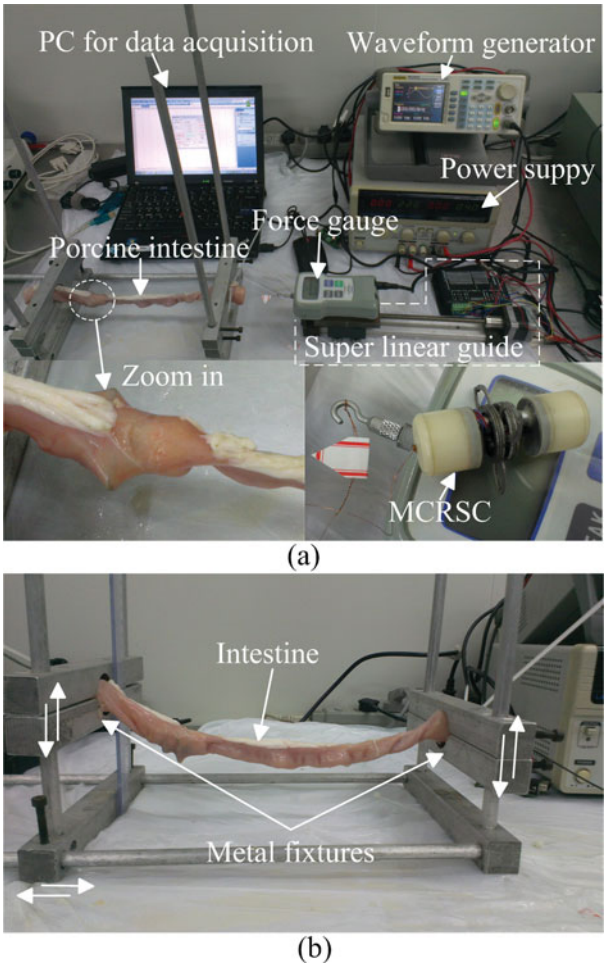

Fig. 10. The *ex vivo* experiments: (a) measuring the anchoring force, and (b) testing the locomotion performance.

drag MCRSC, which was placed in the intestinal sample, at a constant low speed of 0.5 mm/s, and this speed was regulated by the frequency of sine wave generated by a waveform generator. The measurements were sent to a PC through a serial port and recorded by the appendant software of force gauge. Here we used two cylinders made from ABS to substitute for camera and 3D receiving coil. In addition, the sliding clamper was required to fully expand its legs before the dragging began.

We conducted this testing in the intestinal samples with diameters of 19.7, 21.3, and 23.2 mm, and the corresponding measurements of the anchoring force were 1053, 974, and 847 mN. The anchoring force clearly decreased with the intestinal diameter. Adopting the peristaltic force of 17.2 g/cm estimated by Miftahof,[38] we calculated the required value of anchoring force as 688 mN for 40-mm long MCRSC. Considering that the lumen diameter of the colon was typically 20–30 mm, and the compression on the colon from the abdominal fat could further increase the anchoring force, we concluded that the anchoring force could resist intestinal peristalsis.

4.2.2. Testing of locomotion performance. As shown in Fig. 10(b), the locomotion performance of MCRSC was tested in freely suspended intestines; the middle segment (about 10 cm in length) was selected as a crawling environment because the angle of slope of this region could be considered constant, and the change in biomechanical properties caused by the fixtures was negligible. In this testing, the MCRSC was connected to external power using wires because the metal fixtures would seriously influence WPT.

We first tested locomotion performance in the horizontal intestine with an initial diameter of 21.4 mm. In particular, we carefully observed the phenomena in steps (a) and (b) because the intestinal tissue might be deformed and folded into MCRSC during this stage as a result of friction between the sliding clamper and the intestinal wall. Slight local deformation in the intestinal tissue was observed,

https://doi.org/10.1017/S0263574715000697 Published online by Cambridge University Press

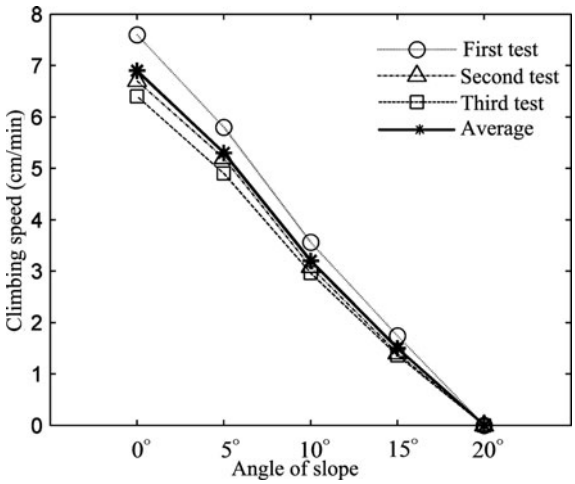

Fig. 11. Climbing speeds in the first, second, and third tests when the angle of slope increases from 0°to 20°(5°interval), and their averages.

but the phenomenon of tissue getting folded into MCRSC never occurred. Two factors may explain this: first, the periodic stroke of MCRSC was only 8.5 mm, and hence the length of tissue that might be folded into MCRSC was short; second, the friction was small because the diameter of the sliding clamper (13.62 mm) was smaller than that of the body (14 mm). The locomotion speed averaged 6.6 cm/min in the horizontal test.

Next, we tested climbing performance in the sloping intestine with an initial diameter of 19.6 mm. The experiment setup for this testing was identical to those shown in Fig. 10(b), and the angle of slope could be changed by adjusting relative height between two fixtures. Note that the straight-line distance between two fixtures should be constant to avoid changing the intestinal lumen environment by stretching or shrinking the intestine. Hence, the horizontal and vertical distances between the two fixtures must be adjusted simultaneously when the angle of slope was changed.

We started with a 0°angle and increased by 5°for each new experiment. In each experiment, we first controlled MCRSC to move its sliding clamper (in a fully leg-retracting state) back and forth to determine max β_1 (i.e., the maximum angle of slope for no slipping), and then controlled MCRSC to climb up in order to determine max β_2 (i.e., the maximum angle of slope for positive net stroke). Climbing was considered to have failed if the MCRSC was not able to advance by 5 cm within 10 min. Slipping began when the angle of slope was 35°, and the climbing failed when the angle of slope was 20°. Consequently, we inferred that max β_1 and max β_2 ranged from 30–35°and 15–20°, respectively.

The above test was repeated thrice and lasted for about 90 min. Figure 11 shows the climbing speed for each testing, we found that the climbing speed in the first, second, and third tests decreased in sequence, which was because the excised intestine stiffened with time, although it was often humidified. Stroke loss became more significant as the angle of slope increased, and the climbing speed declined rapidly, with average of 6.9, 5.3, 3.2, 1.5, and 0 cm/min for 0, 5, 10, 15, and 20°angles, respectively. To summarize, stroke loss L_1 in step (b) was negligible for all angles of slope; stroke loss L_2 in step (d) was observed for all angles of slope, which became increasingly significant as the angle of slope increased and accounted for the main stroke loss; stroke loss L_3 was much smaller than L_2 and became observable from a 15°angle. The main reason for the climbing failure was that the current periodic stroke S_T was too small to overcome stroke loss in a locomotion cycle; therefore, a larger S_T should be adopted in future designs.

Based on the above results (i.e., max β_1 was much larger than max β_2), we conclude that the climbing performance was not weakened by the absence of anchoring in steps (a) and (b) for the current design. Assuming that the angle of slope could be reduced to less than 5°by adjusting patient postures, we can conservatively estimate an average speed of 5 cm/min for the MCRSC *in vivo*. Given an average length of 1.5 m for the colon, a full inspection would take 30 min, and is thus within a time frame of standard colonoscopy.

https://doi.org/10.1017/S0263574715000697 Published online by Cambridge University Press

5. Conclusions

In this paper, a motor-driven capsule robot based on a sliding clamper, together with its design, kinetic analysis, and testing, has been presented. By carefully designing the gear reducers, the MCRSC basically meets the kinetic requirements of the colon for capsule robots: its leg-expanding time, longitudinal thrust, and minimum leg-expanding force are about 1.13 s, 6.5 N, and 2.964 N, respectively. The sliding clamper, which has an expanding ratio of over 230% and a fully leg-expanding diameter of 32.6 mm, is capable of enabling locomotion, distending collapsed intestinal tissue for better inspection, and holding the MCRSC at suspicious lesions to execute advanced functions. The locomotion performance of MCRSC has also been assessed, and it needs about 30 min to travel through the entire colon having a length of 1.5 m. Thus, the proposed MCRSC is suitable for colon inspection.

Our future work focuses on the design of drug delivery, which is implemented by exploiting the linear motion of sliding clamper to squeeze a soft drug chamber. This is a torus-like drug chamber, and will be placed between the baffle of the gear reducer and the sliding clamper (refer to Fig. 5), and a new overall design will clearly be needed to ensure compatibility. In addition, the point contact between the arc-shaped leg and the intestinal tissue raises the potential of tissue trauma in the present design. To address this safety issue, we plan to add tile-like parts with surface microgroove cushions[39] to the tips of arc-shaped legs to achieve surface contact in the future design. Since higher friction, and hence more stable anchoring, can be achieved by microgroove cushions than the current design of point contact, it can be expected that the locomotion performance of MCRSC will improve.

References

1. G. Iddan, G. Meron, A. Glukhovsky and P. Swain, "Wireless capsule endoscopy," *Nature* **405**, 417–418 (2000).
2. H. Angelita and J. D. Waye, "Complications and hazards of gastrointestinal endoscopy," *World J. Surg.* **13**(2), 193–201(1989).
3. J. Westerhof, R. Weersman and J. Koornstra, "Risk factors for incomplete small-bowel capsule endoscopy," *Gastrointest. Endos.* **69**(1), 74–80 (2009).
4. G. Ciuti, A. Menciassi and P. Dario, "Capsule endoscopy: From current achievements to open challenges," *IEEE Rev. Biomed. Eng.* **4**, 59–72 (2011).
5. S. Yim and M. Sitti, "Design and rolling locomotion of a magnetically actuated soft capsule endoscope," *IEEE Trans. Robot.* **28**(1), 183–194 (2012).
6. S. Yim, K. Goyal and M. Sitti, "Magnetically actuated soft capsule with the multimodal drug release function," *IEEE/ASME Trans. Mechatron.* **18**(4), 1413–1418 (2013).
7. S. Yim, E. Gultepe, D. H. Gracias and M. Sitti, "Biopsy using a magnetic capsule endoscope carrying, releasing and retrieving untethered micro-grippers," *IEEE Trans. Biomed. Eng.* **61**(2), 513–521 (2014).
8. H. Zhou, G. Alici, T. D. Than and W. Li, "Modeling and experimental investigation of rotational resistance of a spiral-type robotic capsule inside a real intestine," *IEEE/ASME Trans. Mechatron.* **18**(5), 1555–1562 (2013).
9. G. Lien, C. Liu, J. Jiang, C. Chuang and M. Teng, "Magnetic control system targeted for capsule endoscopic operations in the stomach-design, fabrication, and *in vitro* and *ex vivo* evaluations," *IEEE Trans. Biomed. Eng.* **59**(7), 2068–2079 (2012).
10. J. D. Gumprecht, T. C. Lueth and M. B. Khamesee, "Navigation of a robotic capsule endoscope with a novel ultrasound tracking system," *Microsyst. Technol.* **19**(9–10), 1415–1423 (2013).
11. K. Harada, D. Oetomo, E. Susilo, A. Menciassi, D. Daney, J. Merlet and P. Dario, "A reconfigurable modular robotic endoluminal surgical system: Vision and preliminary results," *Robotica* **28**(2), 171–183 (2010).
12. P. Valdastri, R. J. Webster, C. Quaglia, M. Quirini, A. Menciassi and P. Dario, "A new mechanism for mesoscale legged locomotion in compliant tubular environments," *IEEE Trans. Robot.* **25**(5), 1047–1057 (2009).
13. M. Quirini, A. Menciassi, S. Scapellato, P. Dario, F. Rieber, C. Ho, S. Schostek and M. O. Schurr, "Feasibility proof of a legged locomotion capsule for the GI tract," *Gastrointest. Endosc.* **67**(7), 1153–1158 (2008).
14. H. M. Kim, S. Yang, J. Kim, S. Park, J. H. Cho, J. Y. Park, T. S. Kim, E. Yoon, S. Y. Song and S. Bang, "Active locomotion of a paddling-based capsule endoscope in *in vitro* and *in vivo* experiments," *Gastrointest. Endosc.* **72**(2), 381–387 (2010).
15. P. Dario, M. C. Carrozza, L. Lencioni, B. Magnani and S. D. Attanasio, "A Micro Robotic System for Colonoscopy," **In**: *Proceedings of the IEEE International Conference on Robotics and Automation*, Albuquerque, NM (Apr. 20–25, 1997), Vol. 2, pp. 1567–1572.
16. P. Dario, P. Ciarletta, A. Menciassi and B. Kim, "Modeling and experimental validation of the locomotion of endoscopic robots in the colon," *Int. J. Robot. Res.* **23**(4–5), 549–556 (2004).
17. M. Karagozler, E. Cheung, J. Kwon and M. Sitti, "Miniature Endoscopic Capsule Robot Using Biomimetic Micro-Patterned Adhesives," **In**: *Proceedings of the First IEEE/RAS-EMBS International Conference*

https://doi.org/10.1017/S0263574715000697 Published online by Cambridge University Press

on Biomedical Robotics and Biomechatron.'06 (BioRob'06), IEEE, Pisa (Feb. 20–22, 2006), pp. 105–111.
18. W. Lin, Y. Shi, Z. Jia and G. Yan, "Design of a wireless anchoring and extending micro robot system for gastrointestinal tract," *Int. J. Med. Robot. Comp.* **9**(2), 167–179 (2013).
19. W. Chen, G. Yan, Z. Wang, P. Jiang and H. Liu, "A wireless capsule robot with spiral legs for human intestine," *Int. J. Med. Robot. Comp.* **10**(2), 147–161 (2014).
20. W. Chen, G. Yan, S. He, Q. Ke, Z. Wang, H. Liu and P. Jiang, "Wireless powered capsule endoscopy for colon diagnosis and treatment," *Physiol. Meas.* **34**(11), 1545–1561 (2013).
21. L. J. Sliker, M. D. Kern, J. A. Schoen and M. E. Rentschler, "Surgical evaluation of a novel tethered robotic capsule endoscope using micro-patterned treads," *Surg. Endosc.* **26**(10), 2862–2869 (2012).
22. M. Quirini, A. Menciassi, S. Scapellato, C. Stefanini and P. Dario, "Design and fabrication of a motor legged capsule for the active exploration of the gastrointestinal tract," *IEEE/ASME Trans. Mechatron.* **13**(2), 169–179 (2008).
23. M. Simi, P. Valdastri, C. Quaglia, A. Menciassi and P. Dario, "Design, fabrication, and testing of a capsule with hybrid locomotion for gastrointestinal tract exploration," *IEEE/ASME Trans. Mechatron.* **15**(2), 170–180 (2010).
24. Z. Jia, G. Yan, Z. Wang and H. Liu, "Efficiency optimization of wireless power transmission systems for active capsule endoscopes," *Physiol. Meas.* **32**(10), 1561–1573 (2011).
25. B. S. Terry, A. C. Passernig, M. L. Hill, J. A. Schoen and M. E. Rentschler, "Small intestine mucosal adhesivity to *in vivo* capsule robot materials," *J. Mech. Behav. Biomed.* **15**, 24–32 (2012).
26. M. D. Kern, J. O. Alcaide and M. E. Rentschler, "Soft material adhesion characterization for *in vivo* locomotion of robotic capsule endoscopes: Experimental and modeling results," *J. Mech. Behav. Biomed.* **39**, 257–269 (2014).
27. Shenzhen Winner Mechanical and Electrical Co., (Feb. 2015). [Online]. Available at: http://www.autotrd.com/sell/show.php?itemid=1316
28. S. Park, K. Koo, S. M. Bang, J. Y. Park, S. Y. Song and D. D. Cho, "A novel microactuator for microbiopsy in capsular endoscopes," *J. Micromech. Microeng.* **18**(2), 1–9 (2008) 025032.
29. S. P. Woods and T. G. Constandinou, "Wireless capsule endoscope for targeted drug delivery: Mechanics and design considerations," *IEEE Trans. Biomed. Eng.* **60**(4), 945–953 (2013).
30. V. D. Graaff and K. Marshall, *Human Anatomy* (McGraw-Hill, New York, NY, 2002).
31. C. Zhang, H. Liu, R. Tan and H. Li, "Modeling of velocity-dependent frictional resistance of a capsule robot inside an intestine," *Tribol. Lett.* **47**(2), 295–301 (2012).
32. F. Xu and Q. Li, *Precision Machine Design* (Tsinghua University Press, Beijing, China, 2005).
33. R. Carta, G. Tortora, J. Thone, B. Lenaerts, P. Valdastri, A. Menciassi, P. Dario and R. Puers, "Wireless powering for a self-propelled and steerable endoscopic capsule for stomach inspection," *Biosens. Bioelectron.* **25**(4), 845–851 (2009).
34. P. Ciarletta, P. Dario, F. Tendick and S. Micera, "Hyperelastic model of anisotropic fiber reinforcements within intestinal walls for applications in medical robotics," *Int. J. Robot. Res.* **28**(10), 1279–1288 (2009).
35. C. Bellini, P. Glass, M. Sitti and ES. Di. Martino, "Biaxial mechanical modeling of the small intestine," *J. Mech. Behav. Biomed.* **4**(8), 1727–1740 (2011).
36. D. Zarrouk, I. Sharf and M. Shoham, "Analysis of wormlike robotic locomotion on compliant surfaces," *IEEE Trans. Biomed. Eng.* **58**(2), 301–309 (2011).
37. H. D. Hoeg, A. B. Slatkin, J. W. Burdick and W. S. Grundfest, "Biomechanical Modeling of the Small Intestine as Required for the Design and Operation of a Capsule Robot," **In**: *Proceedings of the IEEE International Conference on Robotic Automation*, IEEE, San Francisco, CA (Apr. 24–28, 2000), Vol. 2, pp. 1599–1606.
38. R. N. Miftahof, "The wave phenomena in smooth muscle syncytia," *In. Silico. Biol.* **5**(5), 478–498 (2005).
39. P. Gao, G. Yan, Z. Wang, P. Jiang and H. Liu, "Microgroove cushion of robotic endoscope for active locomotion in the gastrointestinal tract," *Int. J. Med. Robot. Comp.* **8**(4), 398–406 (2012).